Journal of Engineering Mechanics and Machinery (2026)
Clausius Scientific Press, Canada

DOI: 10.23977/jemm.2026.110109
ISSN 2371-9133 Vol. 11 Num. 1

Satellite Clock Offset Prediction Using a Combined Model of GM and RBF Neural Network

Quancheng Wang, Ye Yu*, Guodong Jin, Jianwei Zhao, Xiaoyu Gao, Minli Yao

Rocket Force University of Engineering, Xi'an, 710025, Shaanxi, China
**Corresponding author: yuye115@mails.ucas.edu.cn*

Keywords: BeiDou Satellite Navigation System; clock offset prediction; RBF neural network; grey model; accuracy analysis; stability analysis

Abstract: This study proposes a GM-RBF composite model addressing limitations of standalone GM in satellite clock offset prediction. By synergistically combining GM-based trend extraction with RBF neural network residual modelling, the hybrid approach leverages minimal data requirements while enhancing predictive precision. Utilizing precise BDS ephemeris from Wuhan University, comparative experiments against GM, LPM and QPM benchmarks were conducted. The GM-RBF model achieved substantial improvements in 6-hour forecasting performance, with accuracy gains of 1.25–1.81 ns and stability enhancements of 0.25–1.73 ns. These results validate the superiority of component-based decomposition strategies for navigation satellite clock offset prediction.

1. Introduction

The accuracy of positioning, navigation and timing (PNT) capabilities depends critically on satellite clock offset precision [1-3]. Refined modeling of clock deviations is indispensable for system optimization [4-6], with precise clock offset forecasting particularly crucial for BDS-3's centimeter-level point positioning services [7].

Commonly employed prediction methods include Linear Polynomial Model (LPM), Quadratic Polynomial Model (QPM) and Grey Model (GM). However, limited adaptability across satellite clocks and strong data dependence may introduce significant errors [8-10].

To overcome these constraints, this study introduces a hybrid GM-RBF approach combining GM trend extrapolation with RBF neural network residual modeling. Using precise clock offset data from Wuhan University GNSS Analysis Centre, experiments on eight diverse BDS satellites demonstrate the method's effectiveness and superiority.

2. Construction of the Combined GM and RBF Neural Network Model

2.1. GM Model

The GM forecasting model utilizes accumulation generation and whitening techniques to transform the original nonlinear time series into a near-linear sequence. Particularly advantageous for small-sample forecasting scenarios, this model necessitates only sparse data for reliable model

establishment. The operational mechanism of its algorithm [11-12] is detailed below:

Consider a set of satellite clock offset time series:

$$x^{(0)}=\left\{x^{(0)}(1),x^{(0)}(2),\cdots,x^{(0)}(n)\right\} \tag{1}$$

Construct a single-accumulation generated sequence (1-AGO) for this time series:

$$\begin{aligned} x^{(1)}&=\left\{x^{(1)}(1),x^{(1)}(2),x^{(1)}(3),\cdots,x^{(1)}(n)\right\}\\ x^{(1)}&=\left\{^{(0)}(1),x^{(0)}(1)+x^{(0)}(2),\cdots,x^{(0)}(1)+x^{(0)}(2)+\cdots+x^{(0)}(n)\right\}\end{aligned} \tag{2}$$

where

$$x^{(1)}(k)=\sum_{i=1}^{k}x^{(0)}(i),k=1,2,3,\cdots,n \tag{3}$$

Since the underlying mechanism of the grey model involves exponential growth prediction, the associated mathematical expression is given by:

$$y=a+ce^{b} \tag{4}$$

Formulate a first-order ordinary differential equation with constant coefficients governing the previously established accumulated generating operation sequence of order one (1-AGO):

$$\frac{dx^{(1)}(k)}{dt}+ax^{(1)}t=u,t\in[0,+\infty] \tag{5}$$

In equation (5), the parameter a represents the development coefficient, and the parameter u denotes the grey effect quantity.

To facilitate the solution of a,u, integrating both sides of equation (5) over the interval $[k,k+1]$ yields:

$$\int_{k}^{k+1}\frac{dx^{(1)}(t)}{dt}dt+\int_{k}^{k+1}ax^{(1)}(t)dt=\int_{k}^{k+1}udt,k=1,2,3,\cdots,n-1 \tag{6}$$

Solving both sides simultaneously yields:

$$x^{(1)}(k+1)-x^{(1)}(k)+a\int_{k}^{k+1}x^{(1)}(t)\,dt=u,k=1,2,3,\cdots,n-1 \tag{7}$$

Because:

$$x^{(1)}(k+1)-x^{(1)}(k)=x^{(0)}(k+1) \tag{8}$$

Therefore, equation (7) can be expressed as:

$$x^{(0)}(k+1)+az^{(1)}(k+1)=u,k=1,2,3,\cdots,n-1 \tag{9}$$

In equation (9), $z^{(1)}(k+1)$ is the average of $x^{(0)}(k)$ and $x^{(0)}(k+1)$, and we obtain:

$$z^{(1)}(k+1)=\frac{1}{2}\cdot\left\{x^{(1)}(k+1)+x^{(1)}(k)\right\},k=1,2,3,\cdots,n-1 \tag{10}$$

Expressing (10) in matrix form yields:

$$\begin{bmatrix} x^{(0)}(2) \\ x^{(0)}(3) \\ \vdots \\ x^{(0)}(n) \end{bmatrix} = \begin{bmatrix} -z^{(1)}(2) & 1 \\ -z^{(1)}(3) & 1 \\ \vdots & \vdots \\ -z^{(1)}(n) & 1 \end{bmatrix} \cdot \begin{bmatrix} a \\ b \end{bmatrix} \tag{11}$$

Let:

$$Y = \begin{bmatrix} x^{(0)}(2) \\ x^{(0)}(3) \\ \vdots \\ x^{(0)}(n) \end{bmatrix}, G = \begin{bmatrix} -z^{(1)}(2) & 1 \\ -z^{(1)}(3) & 1 \\ \vdots & \vdots \\ -z^{(1)}(n) & 1 \end{bmatrix} \tag{12}$$

Then, by the method of least squares, the least-squares solution to equation (11) is:

$$\begin{bmatrix} \hat{a} & \hat{u} \end{bmatrix} = \left(G^T G\right)^{-1} G^T Y_n \tag{13}$$

The grey prediction model established using the sequence (1-AGO) generated by the first-order accumulation of the sample yields:

$$\hat{x}^{(1)}(k+1) = \left\{ \hat{x}^{(0)}(1) - \frac{\hat{b}}{\hat{a}} \right\} e^{(-\hat{a}k)} + \frac{\hat{u}}{\hat{a}}, k = 0,1,\cdots,n-1,\cdots \tag{14}$$

where k specifies the number of original data sequences involved in the forecast. With the above model, data sequences at any future time point can be predicted.

2.2. Radial Basis Function Neural Network

A Radial Basis Function (RBF) network is an artificial neural network employing radial basis functions as activation functions. The output of an RBF network is a linear combination of the input radial basis function and the neuron parameters. Generalized regression neural networks represent an enhancement of RBF networks, employing RBFs as the “basis” for the hidden layer space. Input vectors map directly to the hidden space, with no weighted connections required. Once the center points of the RBFs are determined, this mapping relationship is also established.

RBFs constitute three-layer feedforward networks with a single hidden layer. The first layer is the input layer, comprised of signal source nodes. The second layer is the hidden layer, whose number of nodes depends on the requirements of the problem being described. The transformation function of the neurons in the hidden layer is the radial basis function, which is a non-negative, radially symmetric, and decaying function centered on the core point. This function is a local response function, and its specific local response manifests in its transformation from the visible layer to the hidden layer, differing from other networks. Previous feedforward network transformation functions were all global response functions. The third layer is the output layer, which provides the response to the input pattern [13-14]. Its specific structure is illustrated in Figure 1:

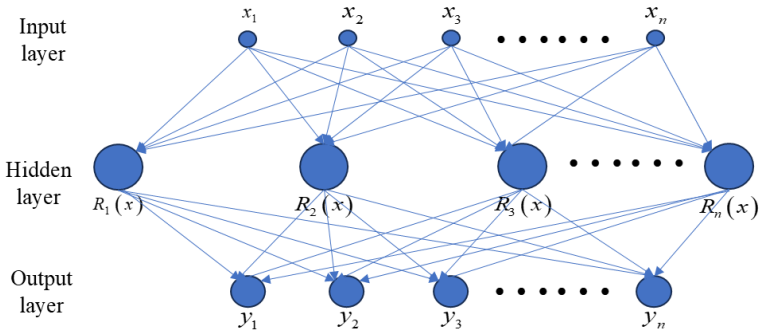

Figure 1: Structural diagram of RBF neural network

The specific operational process is as follows:

First, the centers of the RBF basis functions are determined. The Gaussian function is selected as the RBF kernel function for prediction, as shown in Equation (14):

$$R\left(x_j - c_y\right) = e^{-\left(\frac{\left\|x_j - c_y\right\|}{2\sigma^2}\right)^2} \tag{15}$$

where $\left\|x_j - c_y\right\|$ denotes the Euclidean distance norm, c_y represents the activation function center, σ^2 denotes the variance, and x_j denotes the input vector.

The standard deviation pertaining to the basis function of the hidden layer is thereafter determined as prescribed in Equation (15):

$$\sigma = \frac{d_{\max}}{\sqrt{2k}} \tag{16}$$

where k is the hidden layer node count, and $d_{\max}$ is the maximum center distance. The weight function between the hidden layer and the output layer is solved using the least squares method, as shown in Equation (16):

$$w_{jy} = e^{k\left(\frac{\left\|x_j - c_y\right\|}{c_{\max}^2}\right)} \tag{17}$$

where w_{jy} denotes the weight function between the hidden layer and the output layer.

Finally, the output of the RBF neural network can be determined:

$$x_h = \sum_{i=1}^{k} w_{jy} e^{-\left(\frac{\left\|x_j - c_y\right\|}{2\sigma^2}\right)} \tag{18}$$

where x_h represents the input sample data.

2.3. GM-RBF Combined Model

The GM-RBF combined model employs error compensation as its fundamental principle for model integration, treating satellite clock offset data as comprising two primary components: a trend term and a random term.

Consider a data set as shown in Equation (1). Perform preliminary preprocessing to remove anomalous clock offset values and complete the data sequence using linear interpolation. Employ

the GM model to extract the first data sets for modelling and extrapolation forecasting, thereby obtaining the GM forecast sequence $x^{(0)}$. Taking the remaining data sets, model residuals are calculated and modelled to derive the random component of satellite clock offset data $d^{(0)}$. Using $d^{(0)}$ as the sample set for the RBF neural network, training is conducted to generate extrapolated forecasts, yielding the random component forecast value $\hat{d}^{(0)}$. Finally, the combined forecast value is obtained $y = x^{(0)} + \hat{d}^{(0)}$. The workflow is illustrated in Figure 2:

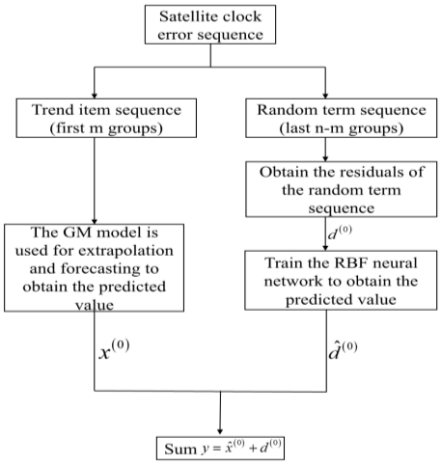

Figure 2: Flowchart of the GM-RBF Model

3. Experiments and Analysis

3.1. Experimental Data Sources

Model validation was performed using precise post-processed BDS satellite clock data from the Wuhan University GNSS Analysis Centre. Data from 17 August 2024 were selected, with a sampling interval of 30 seconds. During this period, 38 BeiDou satellites were in operation, their onboard clocks comprising the following four primary types: GEO-Rb clocks (for geostationary orbit rubidium atomic clocks), IGSO-Rb clocks (for inclined geosynchronous orbit rubidium atomic clocks), MEO-Rb clocks (for Medium Earth Orbit rubidium atomic clocks) and MEO-H clocks (for Medium Earth Orbit hydrogen atomic clocks). To provide comprehensive references for BDS clock offset forecasting, eight satellites representing diverse orbits, clocks, systems and launch years were randomly selected for prediction experiments. These specifically included: BDS-2 GEO-4-Rb PRN04, BDS-2 IGSO-1-Rb PRN06, BDS-2 IGSO-5-Rb PRN10, BDS-3 MEO-4-Rb PRN22, BDS-3 MEO-5-Rb PRN23, BDS-3 MEO-12-H PRN25, BDS-3 MEO-19-H PRN29 and BDS-2 IGSO-3 PRN40, as show in Table 1

Table 1: Selected satellite related information

Satellite ID	Clock type	System	Launch date	Clock offset trend	Linear characteristics
PRN 04	GEO-4-Rb	BDS-2	31 October 2010	Negative values monotonically decreasing	Good
PRN 06	IGSO-1-Rb	BDS-2	17 December 2010	Monotonically increasing	Good
PRN 10	IGSO-5-Rb	BDS-2	2011/12/1	Negative values monotonically decreasing	Good
PRN 22	MEO-4- Rb	BDS-3	12 February 2018	Monotonic increasing	Good
PRN 23	MEO-5-Rb	BDS-3	29 July 2018	Negative values monotonically increasing	Good
PRN 25	MEO-12-H	BDS-3	24 August 2018	Monotonic increasing	Good
PRN 29	MEO-9-H	BDS-3	29 March 2018	Negative values monotonically increasing	Good
PRN 40	IGSO-3-H	BDS-3	5 November 2019	Negative values monotonically decreasing	Good

The variations in the 24-hour precise satellite clock offset time series for these eight satellites on 15 August 2024 are illustrated in Figure 3. Among them, the clock offset time series for satellites

PRN04, PRN10 and PRN40 exhibit a monotonically decreasing trend. Meanwhile, PRN06, PRN22, PRN23, PRN25 and PRN29 show monotonically increasing clock offset trends. All eight satellites demonstrate excellent linear characteristics in their clock offset time series, rendering them fully representative.

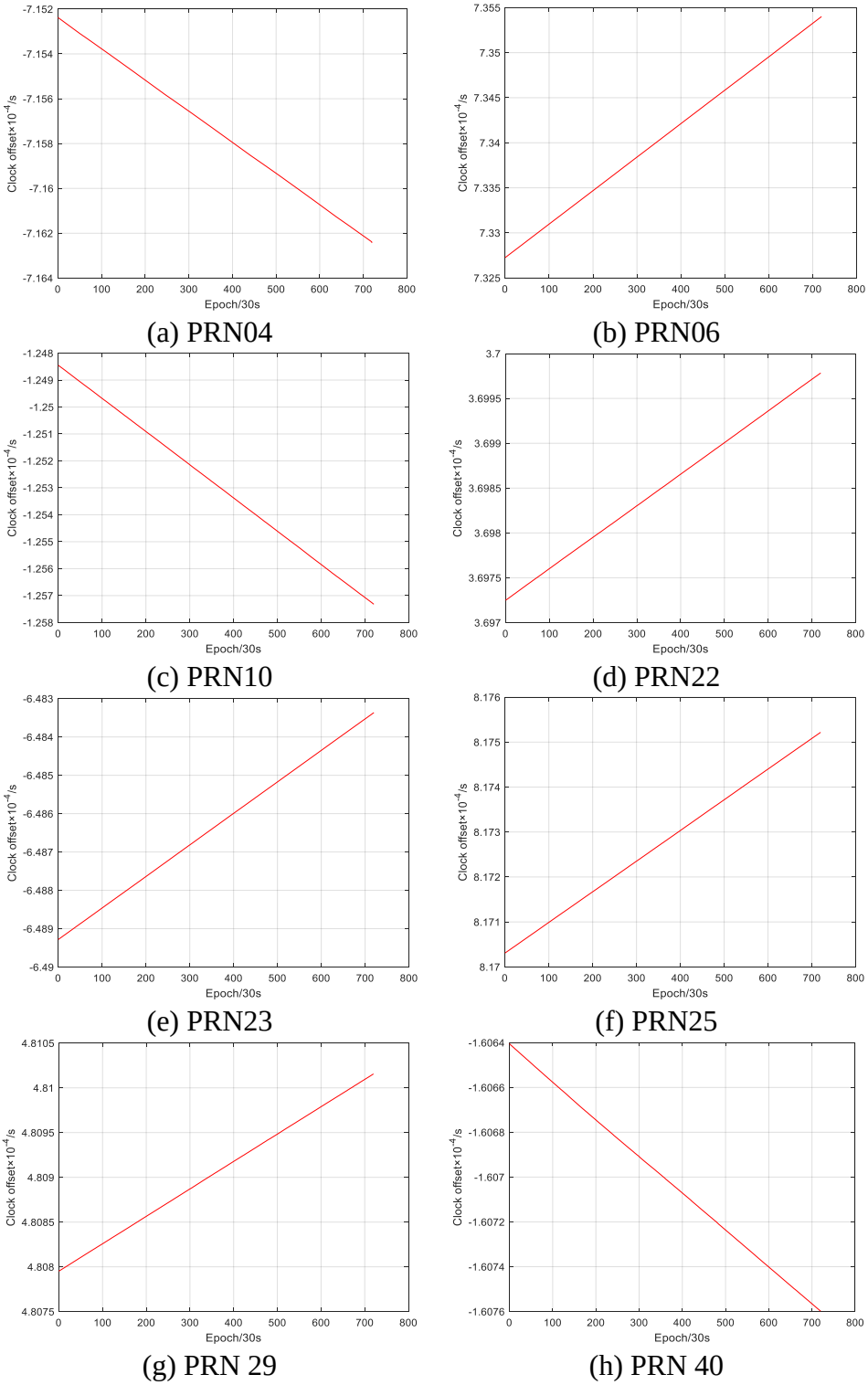

Figure 3: Chart of clock offset variation for the PRN04, PRN06, PRN10, PRN22, PRN23, PRN25, PRN29 and PRN40 satellites

3.2. Forecast Results and Analysis

To evaluate the performance of the satellite clock offset prediction models developed in this study, precise post-processing satellite clock offset data from the BeiDou Navigation Satellite System (BDS) on 4 August 2025 were employed. Satellite clock offset data from the preceding 12 hours were utilized to construct a linear polynomial model (LPM), a quadratic polynomial model (QPM), and a grey prediction model (GM), which were then applied to forecast satellite clock offsets for the subsequent 6 hours. Forecasts were compared with precise satellite clock offset data from the Wuhan University GNSS Analysis Centre for the same period. The forecast errors for each model were calculated, with particular emphasis on determining the improvement rate in forecast accuracy (RMS) of the GM-RBF model relative to the grey forecast model GM. The precise satellite clock offset data released by Wuhan University GNSS Analysis Centre exhibited errors below 0.1 nanoseconds, thus qualifying as "true values". GM-RBF model accuracy was assessed via RMS and Range, as defined in Equations (19) and (20). The magnitude of RMS determines the precision of the model's forecast. A smaller RMS indicates that the model's forecast values are closer to the true values, signifying higher forecasting accuracy. Conversely, a larger RMS indicates a greater discrepancy between the model's forecast values and the true values, signifying lower forecasting accuracy. The Range, meanwhile, reflects the stability of the model's forecasts. A smaller Range indicates a more stable forecasting model; conversely, a larger Range indicates a less stable forecasting model.

$$RMS = \sqrt{\frac{1}{n}\sum_{i=1}^{n}\left(y_i - \hat{y}_i\right)^2} \tag{19}$$

$$Range = \max\left(y_i - \hat{y}_i\right) - \min\left(y_i - \hat{y}_i\right) \tag{20}$$

Forecast error variations and statistical results are shown in Figure 4 and Tables 2–3.

Tables 2–3 and Figures 4–5 collectively demonstrate that GM-RBF-based prediction of satellite clock offsets outperforms the three reference models in terms of error magnitude. Error progression patterns remain qualitatively comparable to the GM baseline yet quantitatively superior. Extended forecast intervals induce initially increasing, subsequently stabilizing absolute errors across most satellites—indicative of the model's improved precision and stability.

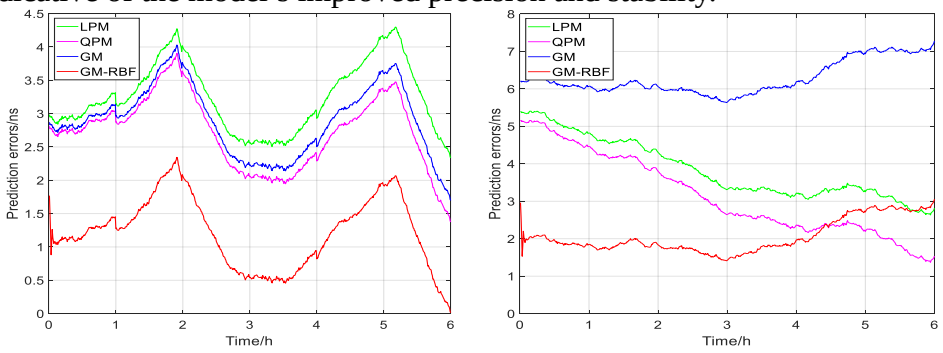

(a) PRN04 (b) PRN06

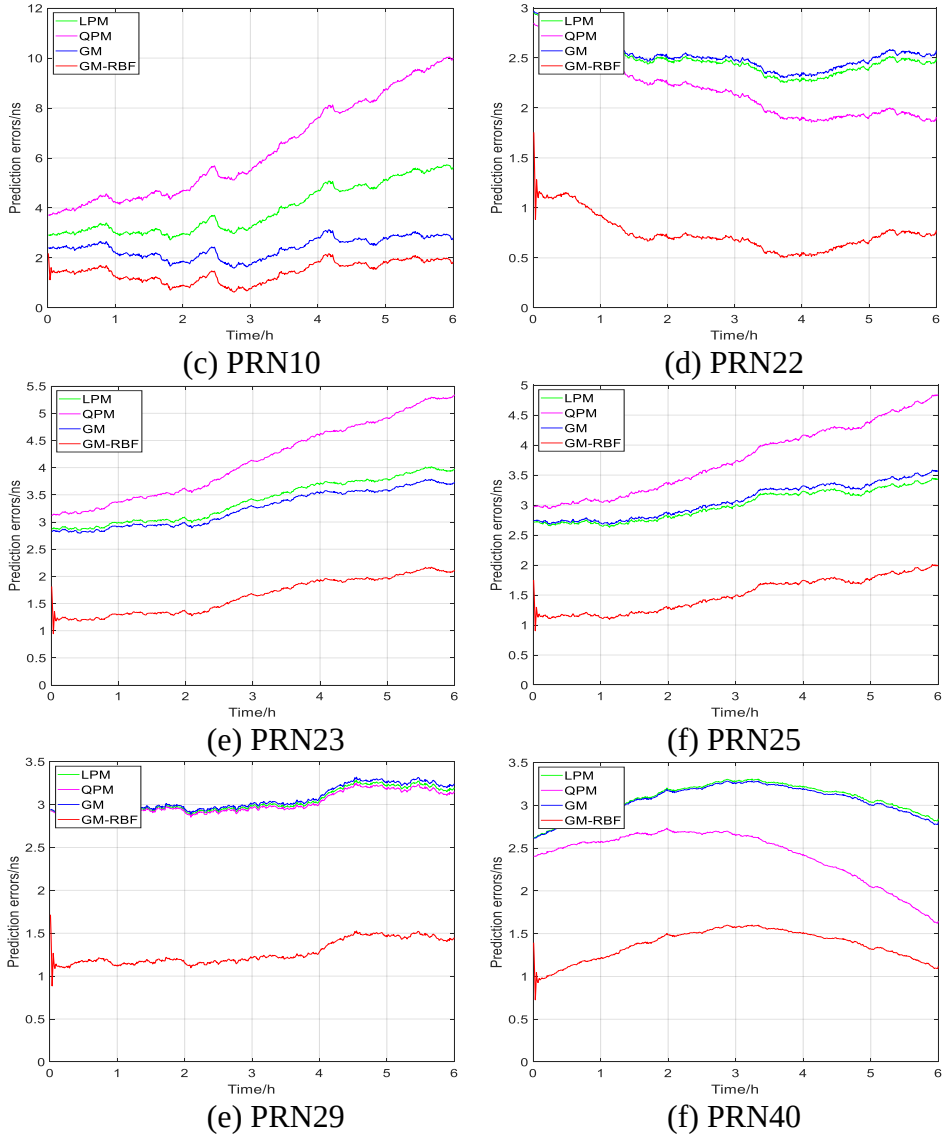

(c) PRN10 (d) PRN22

(e) PRN23 (f) PRN25

(e) PRN29 (f) PRN40

Figure 4: Forecast error variation chart of 6-hour satellite clock offset

Table 2: Statistics of satellite clock offset prediction error and stability (unit: ns)

Model	Evaluation metric	PRN04	PRN06	PRN10	PRN22	PRN23	PRN25	PRN29	PRN40	Mean
LPM	RMS	2.01	3.92	4.05	2.10	3.41	3.01	3.04	3.08	3.13
	Range	2.74	2.77	3.01	0.72	1.17	0.82	0.41	0.69	1.54
QPM	RMS	3.88	3.33	6.62	2.20	4.19	3.81	3.02	2.44	3.69
	Range	4.38	3.79	6.34	0.99	2.22	1.90	0.40	1.11	2.64
GM	RMS	1.67	6.29	2.42	2.55	3.27	3.09	3.07	3.05	3.18
	Range	2.42	1.64	1.54	0.67	0.99	0.91	0.43	0.67	1.16
GM-RBF	RMS	1.12	2.10	1.48	0.77	1.67	1.53	1.28	1.38	1.88
	Range	1.92	1.03	1.12	0.70	0.79	0.70	0.49	0.56	0.91

Table 3: Forecast accuracy improvement rate (relative to GM model)

Satellite	PRN04	PRN06	PRN10	PRN22	PRN23	PRN25	PRN29	PRN40	Average
Improvement (%)	33.06%	66.58%	38.69%	69.94%	48.94%	50.55%	58.28%	54.90%	52.61%

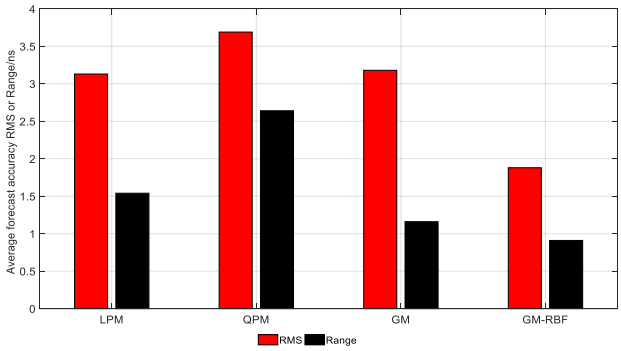

Figure 5: Mean forecast accuracy and mean forecast stability

The predictive capability of the GM-RBF framework was evaluated under operational conditions entailing 12-hour historical data ingestion and 6-hour extrapolation intervals. For the BDS-2 trio, attained accuracies of 1.12 ns, 2.10 ns and 1.48 ns represent improvements of 33.06% (vs. LPM), 66.58% (vs. QPM) and 38.69% (vs. GM). Extending the analysis to the five BDS-3 satellites yielded precision metrics of 0.77 ns, 1.67 ns, 1.53 ns, 1.28 ns and 1.38 ns—with corresponding enhancement magnitudes of 69.94%, 48.94%, 50.55%, 58.28% and 54.90% relative to the GM paradigm. Such performance differentials underscore the marked superiority of the proposed composite architecture.

In terms of forecast stability, the GM-RBF model demonstrated a significant improvement in satellite clock offset prediction stability compared to the other three models. Its average forecast stability increased by 0.63 ns, 1.73 ns and 0.25 ns relative to the LPM, QPM and GM models, respectively. Furthermore, during satellite clock offset forecasting, the combined model exhibits lower range stability for the three satellites equipped with hydrogen masers (PRN25, PRN29, PRN40) than for the five satellites equipped with rubidium clocks (PRN04, PRN06, PRN10, PRN22, PRN23).

4. Conclusion

This study proposes a hybrid GM-RBF model combining GM with RBF neural networks for enhanced satellite clock offset forecasting. Leveraging trend and random components in historical data, the approach accounts for temporal variations and clock type heterogeneity. Experimental results demonstrate superior accuracy compared to QPM, LPM and standard GM models. As evidenced in Figures 4-5 and Tables 2-3, the GM-RBF model exhibits slower error growth and enhanced stability, yielding more reliable predictions. Notably, hydrogen-atom clocks demonstrate superior forecast stability over rubidium counterparts, highlighting the model's adaptability to diverse clock technologies.

Acknowledgements

This study is supported by the National Natural Science Foundation of China (No. 12403080), the China Postdoctoral Research Performance Evaluation and Assessment Funding Project (YJC20251197), the China Postdoctoral Science Foundation Funded Project (No.2024M764304), the Postdoctoral Fellowship Program of CPSF (No. GZC20233565) and the Natural Science Basic Research Program in Shaanxi Province of China (No.2023-JC-QN-0027).

References

[1] Liu W C, Zhou Z G. Research on combined prediction models for GPS satellite clock errors. Surveying and

Mapping with Spatial Information,2023, 46(10), 118–120+124+127.
[2] Yu Y, Huang M, Duan T, et al. Satellite clock offset prediction using a particle swarm optimisation-weighted grey regression combination. Journal of Harbin Institute of Technology, 2020, 52(10): 144-151.
[3] Li M, Huang T, Li W, et al. Precise point positioning with mixed single- and dual-frequency GNSS observations from Android smartphones considering code-carrier inconsistency[J]. Advances in Space Research,2024,74(6): 2664-2679.
[4] Yu Y, Huang M, Wang X Q, et al. Navigation satellite clock offset prediction using grey model improved by least squares method[J]. Bulletin of Surveying and Mapping, 2019, (04):1-6.
[5] Wu Y W, Zhu X W, Gong H, et al. Conceptualisation and considerations for establishing a GNSS time reference [J]. Chinese Journal of Electronics, 2017, 45(08):1818-1826.
[6] Chen Y B, Wang H, Rao Q. Research on GNSS/INS data time synchronisation method based on ZYNQ platform [J]. Microwave Journal, 2023, 39(S1):401-404.
[7] Zhang J, Zhou W, Xuan Z Q, et al. Selection method and performance analysis of periodic terms in satellite clock error prediction models [J]. Acta Astronomica Sinica, 2013, 54(03): 282-290.
[8] Yu Y, Yang C P, Ding Y, et al. A hybrid short-term prediction model for BDS-3 satellite clock bias supporting real-time applications in data-denied environments[J]. Remote Sensing, 2025,17(16):2888-2913.
[9] Wang Y P, Lv Z P, Gong X C, et al. Analysis and comparison of forecast performance among several satellite clock offset prediction models [J]. Geodesy and Geodynamics, 2015, 35(03): 373-378.
[10] Tang Y, Li Y, Li T. Short-term forecasting of BDS-3 satellite clock offsets based on a GM-RBF combined model [J]. Science and Technology Information, 2024, 22(07): 27-31.
[11] Yu Y, Huang M, Wang C Y, et al. A new BDS-2 satellite clock bias prediction algorithm with an improved exponential smoothing method [J], Applied Sciences,2020,10(21):7456-7479.
[12] Mei C S, Huang H J, Jiang K, et al. Application of a level-ratio discrete grey model in satellite clock error forecasting [J]. Journal of Wuhan University (Information Science Edition), 2021, 46(08): 1154-1160.
[13] Yu Y, Huang M, Duan T, et al. Enhancing satellite clock bias prediction accuracy in the case of jumps with an improved grey model[J]. Mathematical Problems in Engineering, vol 2020, Article ID 8186568, 11 pages, 2020.
[14] Jiang F X, Jin S. Satellite clock offset forecasting based on MEA-RBF neural network [J]. Beijing Surveying and Mapping, 2025, 39(11): 1587-1593.